



## Label-free highly multimodal nonlinear endoscope

D Septier, V Mytskaniuk, R Habert, D Labat, K Baudelle, Matteo Conforti,  
G Brévalle-Wasilewski, G Bouwmans, H Rigneault, Alexandre Kudlinski

### ► To cite this version:

D Septier, V Mytskaniuk, R Habert, D Labat, K Baudelle, et al.. Label-free highly multimodal nonlinear endoscope. Optics Express, 2022, 30, 10.1364/oe.462361 . hal-03706852

**HAL Id: hal-03706852**

**<https://hal.science/hal-03706852>**

Submitted on 28 Jun 2022

**HAL** is a multi-disciplinary open access archive for the deposit and dissemination of scientific research documents, whether they are published or not. The documents may come from teaching and research institutions in France or abroad, or from public or private research centers.




L'archive ouverte pluridisciplinaire **HAL**, est destinée au dépôt et à la diffusion de documents scientifiques de niveau recherche, publiés ou non, émanant des établissements d'enseignement et de recherche français ou étrangers, des laboratoires publics ou privés.



Distributed under a Creative Commons Attribution 4.0 International License



# Label-free highly multimodal nonlinear endoscope

D. SEPTIER,<sup>1</sup> V. MYTSKANIUK,<sup>2</sup> R. HABERT,<sup>1</sup> D. LABAT,<sup>1</sup> K. BAUDELLE,<sup>1</sup> A. CASSEZ,<sup>1</sup> G. BRÉVALLE-WASILEWSKI,<sup>2</sup>  M. CONFORTI,<sup>1</sup>  G. BOUWMANS,<sup>1</sup> H. RIGNEAULT,<sup>2,3</sup> AND A. KUDLINSKI<sup>1,\*</sup> 

<sup>1</sup>Univ. Lille, CNRS, UMR 8523 - PhLAM - Physique des Lasers Atomes et Molécules, F-59000 Lille, France

<sup>2</sup>Lightcore Technologies, Cannes, France

<sup>3</sup>Aix Marseille Univ., CNRS, Centrale Marseille, Institut Fresnel, Marseille, France

\*alexandre.kudlinski@univ-lille.fr

**Abstract:** We demonstrate a 2 mm diameter highly multimodal nonlinear micro-endoscope allowing label-free imaging of biological tissues. The endoscope performs multiphoton fluorescence (3-photon, 2-photon), harmonic generation (second-SHG and third-THG) and coherent anti-Stokes Raman scattering (CARS) imaging over a field of view of 200  $\mu\text{m}$ . The micro-endoscope is based on a double-clad antiresonant hollow core fiber featuring a high transmission window (850 nm to 1800 nm) that is functionalized with a short piece of graded-index (GRIN) fiber. When combined with a GRIN micro-objective, the micro-endoscope achieves a 1.1  $\mu\text{m}$  point spread function (PSF). We demonstrate 3-photon, 2-photon, THG, SHG, and CARS high resolution images of unlabelled biological tissues.

© 2022 Optica Publishing Group under the terms of the [Optica Open Access Publishing Agreement](#)

## 1. Introduction

For an efficient cancer treatment, an early diagnosis is essential. However, the typical strategy involves tissue extraction, sectioning and staining to prepare it for a microscopy interrogation, which is time-consuming and presents a risk of sampling error. In addition, any dynamical information is excluded to such *ex vivo* investigation. For these reasons, an endoscope capable of *in vivo* real-time label-free imaging would provide a faster and less invasive diagnosis alternative. Moreover, such a device would greatly improve decision-making during surgical procedures, in particular for assuring tumor removal and to prevent from relapsing [1].

To overcome the limitation in imaging depth that restricted conventional techniques to shallow tissue layer or to thin sample slices, multiphoton microscopy (MPM) has been implemented as a label-free solution for deep-tissue analysis [2–4]. The simultaneous interaction of two or more photons with the tissues enables to address electronic states of a molecular target via harmonics generation or emission of nonlinear fluorescence, each granting helpful information on the biological tissue, that can be exploited for diagnosis purposes [5–7]. The emission of the nonlinear signals is restricted to the tight focal volume, granting an optical sectioning with a high spatial resolution several hundreds of microns below the sample surface. These effects can be categorized based on the dependence of their efficiency on the power of excitation light. Therefore, in accordance with that, we use the following terminology : second-order processes refer to 2PEF and SHG while third-order processes refer to 3PEF, THG and coherent anti-Stokes Raman scattering (CARS). The fundamental limitation on the imaging depth of second-order nonlinear imaging methods lies in the decrease of signal to noise ratio (SNR) as depth into the sample increases. To overcome this limitation, third-order processes have been exploited to make nonlinear imaging [8–10]. They benefit from a greater excitation localization [11] which leads to a higher SNR deep in the tissue. Moreover, a compromise between tissue scattering and water

absorption points to the optimal excitation wavelengths of 1300 nm and 1700 nm [12], which are too long to reach most fluorophores with 2PEF. For these reasons, 3PEF and THG have been reported to enable high resolution *in vivo* imaging deep in a mouse brain [6,13], unreachable by 2PEF [14–19].

To adapt nonlinear microscopy techniques to micro-endoscopy, the challenge is to miniaturize the bulky MPM optics into a compact and flexible probe. In addition to the optical focusing system, a scanning mechanism is needed in the miniature distal head. The use of microelectromechanical systems (MEMS) scanning mirrors have been reported [18,20], but they lead to a relatively bulky distal end which is not compatible with micro-endoscopy. An alternative is to use a doubly resonant piezoelectric tube of only a few millimeter diameter which provides a spiral scan whose size can be electrically tuned [21,22]. Besides, because nonlinear processes require a high power density, ultrashort pulses (typically sub-ps) are needed. Consequently, the optical fiber of the endoscope needs to deliver ultrashort pulses without distortions for all targeted excitation wavelengths. Despite the difficulty to achieve this, nonlinear micro-endoscopes exploiting second-order processes have been successfully demonstrated over the last decade [23] with performances now approaching the ones of tabletop nonlinear microscopes [24,25]. Several strategies can be employed to do that. This can be done for example with sophisticated dispersion and nonlinearity pre-compensation schemes [26,27] or much simpler integrated ones [28,29] or using hollow core fibers [30,31]. Nowadays, with the rapid development of fiber-based sources and speciality optical fibers, it is also possible to make multimodal micro-endoscopes combining second-order processes and CARS [30,32,33].

Regarding 3PEF micro-endoscopy, the constraints are even stronger because, due to the lower probability of simultaneous absorption of three photons, pulses of higher peak power (and therefore duration shorter than 100 fs typically) are required while keeping a low average power to avoid tissue burning. For those reasons, although benchtop 3PEF microscopes are now well spread in laboratories, adapting this modality into a miniature endoscope remains a challenge. First attempts of miniaturization considered fiber-based light sources [12,15,19,34], but the imaging is done through a bulky microscope objective, thus losing the compactness and flexibility advantages of micro-endoscopy. In [35], the authors developed a miniature multiphoton endoscope using solitons generated at a fixed wavelength of 1700 nm directly in the endoscopic solid core fiber. However, due to the fixed wavelength, the system was not highly multimodal. Additionally, the relatively low energy of the source does not offer the possibility of imaging unlabeled biological tissues. In 2020, Klioutchnikov *et al.* [18] pushed it a step forward by developing a head mounted 3PEF microscope based on a hollow core fiber allowing mouse deep brain imaging. However, the distal head was relatively bulky (> 1 cm in diameter), restricting its use for this specific application.

In this work, we demonstrate the first flexible nonlinear micro-endoscope capable of second-order (2PEF and SHG), third-order (3PEF and THG) as well as CARS nonlinear imaging on unlabeled biological tissues. This highly multimodal imaging micro-endoscope is based on an antiresonant hollow core fiber allowing to deliver < 100 fs pulses from 850 nm to 1800 nm, and featuring a large silica double clad enabling efficient nonlinear signal collection. The distal tip of the fiber is functionalized with a GRIN fiber that allows, when coupled with a miniature GRIN objective, a 1.1  $\mu\text{m}$  spot size for high-resolution imaging. The functionalized fiber is mounted into a 1.5 mm outer diameter resonant piezo scanner featuring active braking that allows to reach 10 frames/s over a field of view of 200  $\mu\text{m}$ . We illustrate the highly multimodal imaging capability of the developed micro-endoscope on various unlabeled biological tissues including mouse brain, mouse skin, mouse retina, ox liver and human colon.

## 2. Double clad hollow core fiber

The choice of the optical fiber is crucial in designing a multimodal endoscope. For the system to allow nonlinear imaging, the fiber must deliver intense and ultrashort pulses without any significant temporal nor spectral distortion. This is even more critical for third-order processes, which require higher power and shorter pulse duration. Moreover, for multimodality purposes, the transmission band must be quite large, as 2PEF typical excitation wavelengths are in the 850 nm to 1000 nm range, and their third order counterparts are ranging up to 1700 nm [36]. Kagomé and tubular antiresonant hollow core fibers are well suited for that [30,31,37], since they present large transmission bands as well as low group velocity dispersion (GVD) and nonlinearity. Here, we have chosen a tubular design for its simplicity and its ability to adjust the guidance properties by tuning the geometrical parameters [38–40]. Figure 1(a) shows the antiresonant fiber fabricated with a stack and draw process, with a close-up view in the core region at the bottom. It has a 45  $\mu\text{m}$  diameter hollow core surrounded by 8 capillaries of 15  $\mu\text{m}$  inner diameter and 425 nm thickness. It is based on the design proposed in [31], but we carefully adjusted these geometrical parameters, in particular the capillary wall thickness, to allow single mode transmission from 850 nm to more than 1800 nm, following the design rules from [40]. The measured attenuation spectrum is represented by the blue line in Fig. 1(b). It was measured by a cutback from 19 to 2 m using a supercontinuum source. Propagation losses are ranging down from 1 to about 0.5 dB/m in the 850–1200 nm range, and are almost constant at 0.5 dB/m over the whole 1200–1800 nm range. The GVD was measured using the low coherence interferometry method [41] and is less than 2 ps/nm/km all over this spectral band, as shown by red markers (measurement) and red solid line (simulations, with the model from [42]).

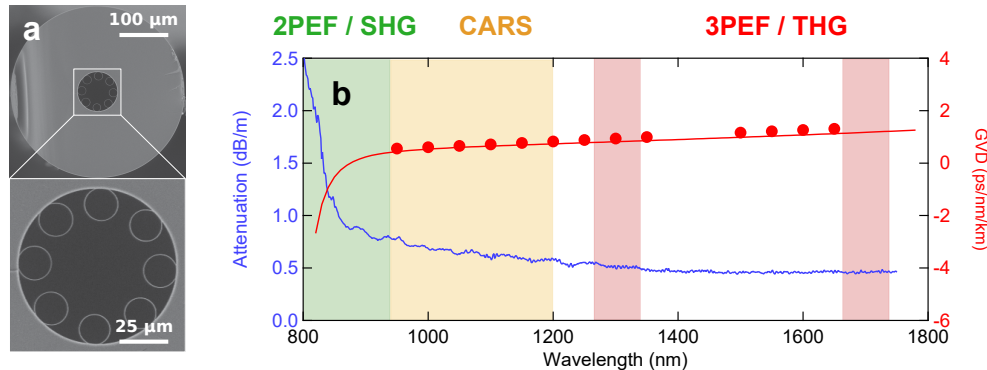


**Fig. 1.** (a) Scanning electron micrographs of the double clad antiresonant hollow core fiber (DC-HCF). Bottom: close-up view on the core region. (b) Measured attenuation spectrum (blue line), GVD (red dots) and simulated GVD (red solid line) over the first transmission band, for a 2 m long DC-HCF.

In addition, the fabricated fiber has a large silica cladding (300  $\mu\text{m}$  in diameter) surrounding the hollow core and guiding light via total internal reflection at the interface with a thin layer of low index polymer (not shown on the pictures in Fig. 1(a)). The surface of the silica double clad is 70,000  $\mu\text{m}^2$  and its numerical aperture (NA) was measured using the method described in [31]. The measured NA value is 0.38 at 450 nm, which ensures an excellent nonlinear signal collection.

## 3. Functionalization of the fiber distal tip

Although these advantages make antiresonant hollow core fibers particularly suited for nonlinear endoscopy applications, the mode full width at half maximum (FWHM) value was measured to be 22  $\mu\text{m}$  at 900 nm (blue dots in Fig. 2(a)), corresponding to a 37.3  $\mu\text{m}$  mode field diameter



(MFD), which is inappropriate for high resolution nonlinear imaging. Therefore, the output mode of the fiber needs to be strongly reduced before being re-imaged onto the sample with a distal micro-objective.

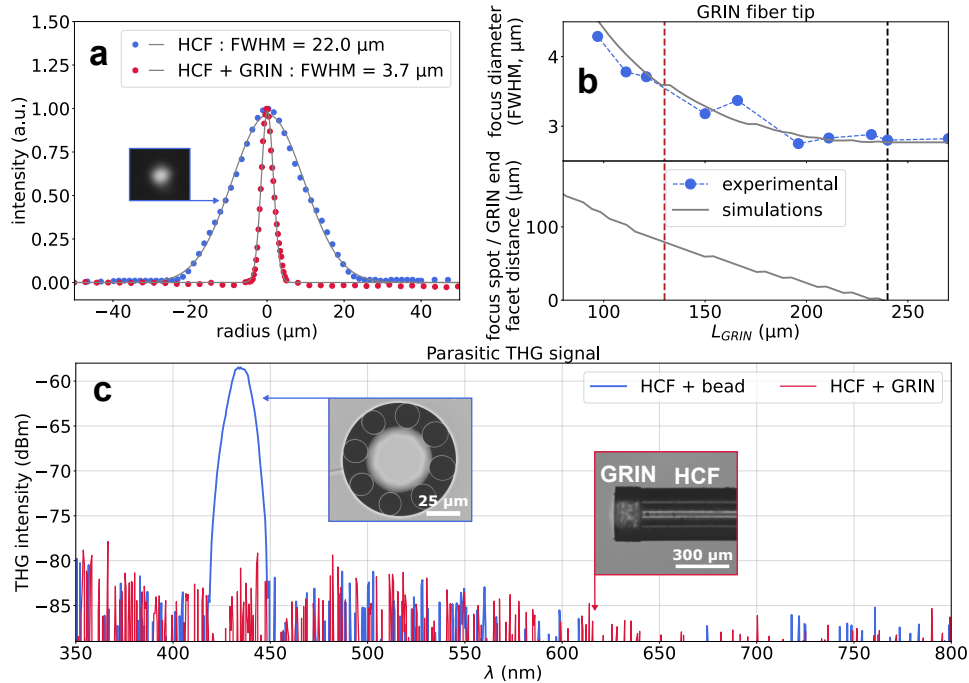


**Fig. 2.** (a) Measured mode size at the output of the hollow core fiber alone (blue dots) and with the GRIN fiber spliced (red dots) at  $\lambda = 900$  nm. Inset: image of the mode. (b) Measured (blue dots) and simulated (gray line) FWHM spot size as a function of the spliced GRIN fiber length, and simulated distance between the focal spot and the GRIN fiber endface. The vertical black dashed line corresponds to half the self-imaging period. The vertical red dashed line corresponds to the actual length of the GRIN fiber used to suppress parasitic THG. (c) Parasitic THG spectrum at the output of the fiber functionalized with a silica bead (blue) and with a 125  $\mu\text{m}$  GRIN fiber of optimized length (red) (see corresponding insets), for a pump wavelength of  $\lambda = 1300$  nm, with 60 fs and 1.2  $\mu\text{J}$  pulses.

One way to do so is to seal a silica bead directly into the hollow core of the fiber [30,31]. The bead then acts as a ball lens, creating a photonic nanojet [43,44] and allowing a focus to a near diffraction limited spot size. Although this works efficiently for second-order nonlinear imaging [31] and CARS imaging [30], problems arise when using higher power and shorter pulses required for third-order nonlinear imaging. Indeed, the extremely high peak power density which is reached at the silica bead/air interface enables strong THG from the interface itself, as evidence by the intense peak observed in Fig. 2(c) for a pump wavelength of 1300 nm. Although it is not critical when targeting second-order nonlinear effects due to the lower peak power required, this THG signal generated in the silica bead is highly detrimental for 3PEF and THG imaging. Firstly, it generates linear fluorescence in the tissue in the same spectral range as 3PEF. Secondly, it can be misinterpreted as THG generated from the tissue to be imaged. In both cases, it results in a noise actually much stronger than the nonlinear signals to be detected. Besides this critical issue, this solution presents other drawbacks. Indeed, the very high divergence of the beam after the bead [31] induces beam clipping inside the endoscopic head, resulting in a significant power loss. Additionally, the hollow structure of the fiber can not be sealed, and is

then prone to air humidity which can cause propagation disturbance. It also makes it hard, if not impossible to clean the fiber tip if needed. Finally, even sealed to the tubes, the bead as a chance to detach itself, especially with the resonant spiral scanning of the fiber.

An alternative solution to shape the output mode of the fiber is to replace the bead by a GRIN fiber spliced to the output end of the hollow core fiber. By exploiting the self-imaging mechanism in GRIN fibers [45], the output mode size can be easily tuned by accurately adjusting the GRIN fiber length. This solution allows shaping the output mode as well as closing up the whole hollow region, avoiding previously mentioned issues. A commercial germanium-doped preform is drawn to a 60  $\mu\text{m}$  core diameter GRIN fiber ( $30 \times 10^{-3}$  refractive index difference) then spliced with a CO<sub>2</sub> laser fiber splicer (Fujikura LZM-100) to the double clad hollow core fiber and cleaved a few hundreds of  $\mu\text{m}$  from the splice (see photo in the insight of Fig. 2(c)). Lastly, successive polishing of the GRIN fiber facet allow to adjust finely its length, measured with an optical microscope. The gray solid line in Fig. 2(b) shows the FWHM spot size as a function of GRIN fiber length, simulated using the model in [46]. The minimum spot size of 2.8  $\mu\text{m}$  (FWHM) is obtained for a GRIN fiber length of 240  $\mu\text{m}$ , which corresponds to half the self-imaging period for this specific fiber. In this case however, the focus is obtained exactly on the GRIN fiber output face, which generates a strong parasitic THG signal (not shown here), similarly to the case of the silica bead described above. To avoid this, it is possible to further reduce the GRIN fiber length which will move the focal spot away from the fiber endface, as shown by the simulated gray solid curve in the bottom graph of Fig. 2(b), while keeping a reasonably small spot size. This is confirmed by measurements of the spot FWHM performed by imaging it on a camera with an optical setup calibrated with resolution targets. The evolution of the spot FWHM measured after successive polishings of the GRIN fiber is depicted by markers in Fig. 2(b). We can therefore choose the best compromise between small spot size and large distance between the fiber endface and the focal spot. After several tries, we found out that for a GRIN fiber length of 130  $\mu\text{m}$  corresponding to a spot FWHM of 3.7  $\mu\text{m}$  (see measurement with red markers in Fig. 2(a)) located 80  $\mu\text{m}$  away from the GRIN fiber end face, there was no measurable parasitic THG signal, as attested by the noise floor measurement represented by the red line in Fig. 2(c). This functionalized fiber is thus well suited for third-order nonlinear imaging.

#### 4. Endoscope assembly and characterization

The micro-endoscope is made of a 2 m long double clad hollow core fiber functionalized with a GRIN fiber as described above, resulting in a FWHM focal spot of 3.7  $\mu\text{m}$ . It is then re-imaged with a miniature GRIN objective (GRINTECH GmbH, GT-MO-070-016-ACR-VISNIR-30-20), to obtain a final point spread function (PSF) of 1.1  $\mu\text{m}$  FWHM at a wavelength of 920 nm, represented in Fig. 3(c). The same endoscopic fiber was used for all results of this work.

The scanning system is a miniature doubly resonant piezoelectric tube (Physik Instrumente), similar to the ones used previously in Refs. [21,26,30]. Using appropriate frequency and phase of driving electric signals (see details in Refs. [26,30]), the fiber tip, and thus the output spot, follow an expanding spiral pattern on the sample. It results in an electrically tunable field of view (FoV) of up to 200  $\mu\text{m}$  (after demagnification by the GRIN objective). The resonant frequency of the fiber (about 1800 Hz) enables high resolution imaging with a high acquisition rate. For example, at 10 frames per second (fps), the distance between two consecutive circles of the spiral is about 560 nm, which is much smaller than the spatial resolution limit imposed by the PSF. As schematically shown in Fig. 3(a), the piezoelectric tube, the fiber distal tip and the miniature objective are encased in a distal head (see picture in Fig. 3(b)). The tube is 3 mm large and 35 mm long, with a 7 mm long section of 2 mm diameter at the end of distal tip. It is made of bio-compatible stainless steel tube, that ensures the compactness and robustness of the distal head.

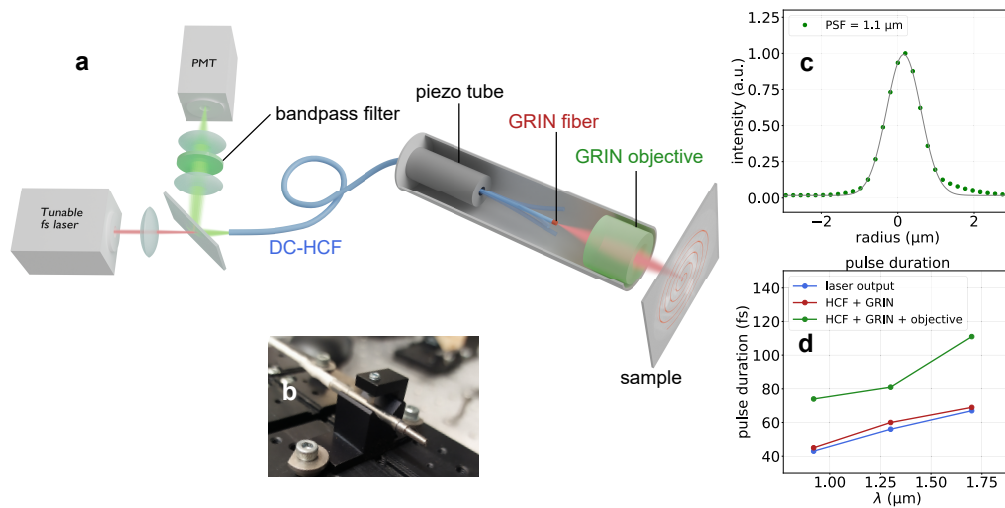


**Fig. 3.** (a) Endoscopy setup scheme, with an inside view and (b) photo of the endoscopic head. (c) Measured points and Gaussian fit (gray line) of the PSF at the output of the full endoscope (hollow-core fiber, spliced GRIN fiber and GRIN micro-objective) for a wavelength  $\lambda = 920$  nm. (d) Measured pulse duration before (blue) and after (red) propagation in a 2 m long fiber with a spliced GRIN lens, and at the output of the endoscope (hollow-core fiber, GRIN fiber and GRIN objective, green).

This micro-endoscope is used for multimodal nonlinear imaging with the experimental setup shown in Fig. 3(a). The tunable femtosecond laser system is made of an ytterbium doped master oscillator power amplifier (Monaco, Coherent) pumping a broadband optical parametric amplifier (Opera-F, Coherent). It provides 40 to 80 fs pulses with an energy up to a few  $\mu\text{J}$ , at a repetition rate of 1 MHz. They are tunable in the ranges 640-940 nm and 1147-2676 nm. The pump laser is injected into the 2 m long hollow core fiber with a lens of 40 mm focal length and minimum coupling efficiency of 80 % at 920 nm, 1300 nm and 1700 nm. The quality of injection into the fundamental mode is controlled with either a Si or InGaAs camera, in order to avoid spurious light propagation in the double clad. The calibration is performed in real-time with a position sensing detector (PSD) driven by a custom python software to optimize the spiral pattern of the scan. The recorded 2D positions of the output spot allows then to reconstruct images.

The nonlinear signal generated within the sample is back-collected by the silica double clad surrounding the hollow core and separated from the excitation signal with a dichroic mirror at the proximal end of the fiber. It is then collected by a high NA lens and sent to a photomultiplier tube (PMT, H7421-40, Hamamatsu Photonics). A set of bandpass filters placed before the detector allows to spectrally filter the nonlinear signal, thus choosing the modality imaging (2PEF, SHG, 3PEF, THG). The image is then reconstructed and displayed in real-time with a home-made software.

As mentioned above, nonlinear imaging using a third-order modality typically requires  $<100$  fs ultrashort pulses on the sample. In our case, the optical fiber was therefore chosen and designed to allow propagation without dispersion in the targeted range of wavelengths. Figure 3(d) shows measurements of the laser pulse duration before the fiber (blue markers), at the output of the 2 m long hollow core fiber with the GRIN fiber spliced (red markers) and at the output of the full endoscope, i.e., after the GRIN micro-objective (green markers), for all wavelengths of interest in multiphoton imaging. It can be seen that the hollow core fiber with the spliced GRIN fiber almost bring no dispersion, and that most of the pulse broadening comes from the GRIN

micro-objective. Here we used a commercial GRIN micro-objective which was not optimized for our application, so we expect that this can be improved. Note that the impact of the residual dispersion due to the micro-objective could be obviously removed at the cost of introducing a pre-compensation module. Nevertheless, the pulse duration at the output of the full endoscope remains in the range 80-110 fs depending on wavelength, which is short enough to allow efficient third-order nonlinear imaging, as we shall see below.

The impact of fiber curvature on the nonlinear signal generated was also addressed by detecting a 2PEF signal from 2  $\mu\text{m}$  fluorescent beads ( $\lambda_{\text{exc}} = 920 \text{ nm}$ ) and bending the fiber to a 10 cm radius of curvature. When doing so, the signal detected decreased by only 18% (due to a decrease of fiber transmission), still granting a satisfying contrast for imaging applications.

## 5. Two and three photon imaging comparison

The primary aim of the study is the integration of third-order nonlinear processes in a multimodal endoscope. Firstly, we checked the order of the processes relatively to the light intensity by measuring the dependence of the fluorescence signal on the excitation power. Here, a  $565 \pm 66 \text{ nm}$  bandpass filter is preceding the detector so only the fluorescence signal is seen. When exciting a sample of 2  $\mu\text{m}$  diameter fluorescent beads at 920 nm, we obtain a slope of 2.05 for the log-log power dependence (green dots in Fig. 4(a)), confirming the 2PEF process involved. Similarly, a slope of 3.03 (red dots in Fig. 4(a)) is obtained when exciting the same sample at 1300 nm, confirming that the 3PEF process is involved in this case.

We next highlight the advantages of 3PEF over 2PEF imaging. Primarily, because third-order nonlinear processes require a higher power density, the emission localization is highly enhanced in all dimensions. This is emphasized in the transverse plane by the enhancement of spatial resolution when imaging 2  $\mu\text{m}$  fluorescent beads (Figs. 4(c) and (d)) or oak leaves (Figs. 4(f) and (g)). The definition of the structures is increased with 3PEF, compared to 2PEF images, as well as the sharpness of the edges. To assert it, a plot along the white light in Figs. 4(c) and (d) is represented in Fig. 4(e), showing the fluorescence intensity profile of four adjacent beads. We highlight the higher spatial resolution of 3PEF along with the great improvement in signal-to-noise ratio (SNR). This confirms the advantages evidenced in 3PEF benchtop nonlinear microscopy [19,36]. Finally, a demonstration of real-time imaging of 2  $\mu\text{m}$  fluorescent bead at 10 fps is presented in [Visualization 1](#) and [Visualization 2](#) (see [Supplement 1](#)), and emphasizes again the improvement on imaging quality of 3PEF over 2PEF, especially for the investigation of dynamical activities.

Likewise, the improvement in localization for the 3PEF signal leads to a better axial resolution, meaning that the fluorescence signal generated outside the focus plane is greatly reduced. Figure 4(b) shows the fluorescence signal for 2PEF (green dots) and 3PEF (red dots) when moving the endoscope head closer to a 2  $\mu\text{m}$  fluorescent bead. A Gaussian fit is then produced, granting the axial resolution measurement (FWHM). The 2PEF signal has an axial resolution of 14.9  $\mu\text{m}$ , whereas it is significantly reduced to 5.2  $\mu\text{m}$  for the 3PEF process. This is illustrated when imaging optical cleaning paper where some out-of-focus structures, seen with 2PEF especially on the top of Fig. 4(h), are completely absent when using 3PEF (Fig. 4(i)), highlighting the great improvement in optical sectioning for 3PEF. This is also evidenced by videos of 2PEF and 3PEF images on biological samples when varying the imaging depth (see [Supplement 1](#) and corresponding [Visualization 1](#), [Visualization 2](#), [Visualization 3](#), [Visualization 4](#), [Visualization 5](#), [Visualization 6](#), and [Visualization 7](#)).

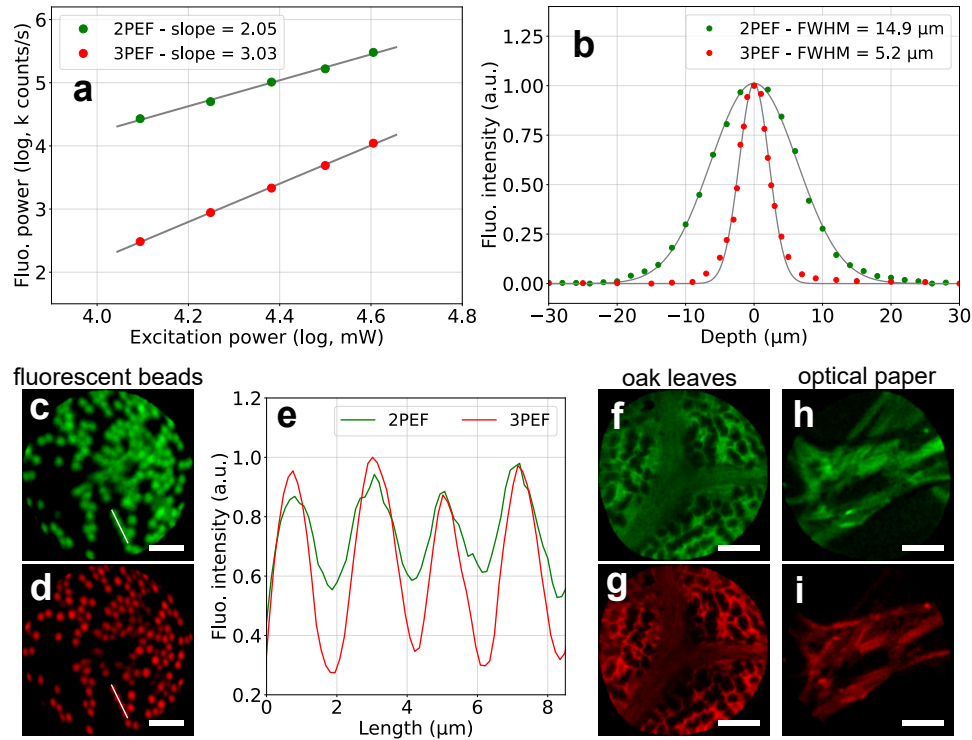


**Fig. 4.** 2PEF ( $\lambda_{\text{exc}} = 920$  nm, represented in green on all sub-figures) and 3PEF ( $\lambda_{\text{exc}} = 1300$  nm, represented in red on all sub-figures) comparison: (a) Dependence of fluorescence signal of 2  $\mu\text{m}$  diameter beads on the excitation power. (b) Axial resolution: measured fluorescence signal when moving the endoscope closer to a 2  $\mu\text{m}$  fluorescent bead and Gaussian fit (gray line). Comparison images of 2  $\mu\text{m}$  fluorescent beads ((c), (d), scale bar is 10  $\mu\text{m}$ , mean power on the sample is 10 mW for 2PEF and 12 mW for 3PEF) with an intensity plot along the white line (e), oak leaves ((f), (g), scale bar is 50  $\mu\text{m}$ , mean power on the sample is 16 mW for 2PEF and 20 mW for 3PEF) and optical cleaning paper ((h), (i), scale bar is 50  $\mu\text{m}$ , mean power on the sample is 15 mW for 2PEF and 14 mW for 3PEF). All images have been acquired with a 2 fps acquisition rate and averaged over 5 images.

## 6. Nonlinear imaging of biological tissues

### 6.1. Sample preparation

Mouse brain, retina and skin samples used in this study were fixed with paraformaldehyde (PFA) before being sliced, and placed between two glass cover-slips for imaging. Brain samples are obtained from a transgenic GFP labeled mouse. All other biological samples imaged here are unstained in order to demonstrate the label-free imaging ability of the endoscope. Fresh human colon biopsies are set in water inside a 1 mm thick spacer, also placed between glass cover-slips.

In order to keep the endoscope head steady during the recording of images, and for ease of use, it was kept horizontal on a 3D-moving stage. The samples were then placed vertically in front of it. This allowed to image in the exact same position on the sample with different parameters or different excitation wavelengths. Images were acquired at a depth of 50 to 150  $\mu\text{m}$  below the surface of the sample, with an average power of 20 to 40 mW on the sample.



### 6.2. Three photon imaging on biological tissues

As stated above, 3PEF has recently been the subject of growing interest in the field of neurology [14–19]. Therefore, we demonstrate in Fig. 5(a) the ability to image neurons inside a mouse brain with our endoscope, at an excitation wavelength of  $\lambda_{\text{exc}} = 1300$  nm. Single cells and some interconnections are distinguishable because of the powerful fluorescence signal generated, whereas a lower background signal allows to set apart the surrounding environment.

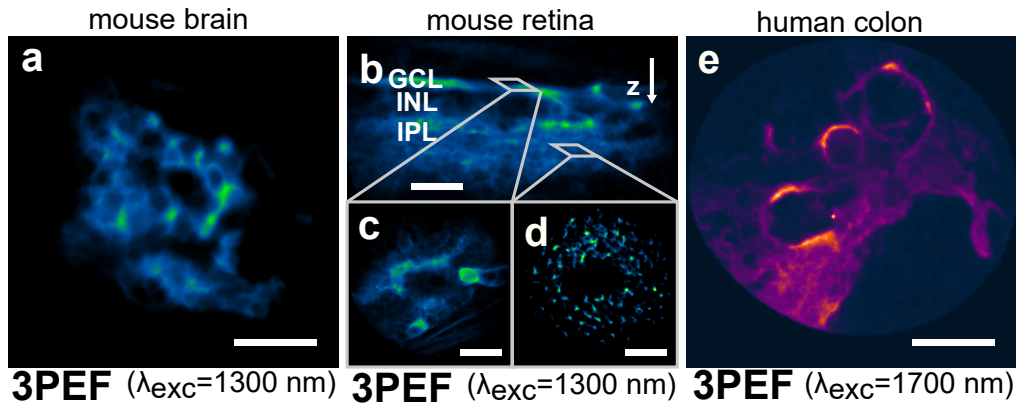


**Fig. 5.** 3PEF images of (a) GFP labeled mouse brain ( $\lambda_{\text{exc}} = 1300$  nm), scale bar is 50  $\mu\text{m}$  and mean power on the sample is 25 mW, (b) unstained mouse retina ( $\lambda_{\text{exc}} = 1300$  nm) radial section, scale bar is 80  $\mu\text{m}$  and mean power on the sample is 29 mW. (c) and (d) are transverse sections in the ganglion cell layer (GCL) and inner plexiform layer (IPL) respectively, scale bar is 50  $\mu\text{m}$ . (e) unstained human colon ( $\lambda_{\text{exc}} = 1700$  nm), scale bar is 50  $\mu\text{m}$  and mean power on the sample is 13 mW. All images have been acquired with a 2 fps acquisition rate and averaged over 10 images.

Moreover, we realize label-free 3PEF imaging of different layers in a mouse retina [47,48] at  $\lambda_{\text{exc}} = 1300$  nm in Fig. 5(b). The ganglion cell layer (GCL) presents the strongest fluorescence emission and enables a great contrast, with a broad range of signals from weak to bright fluorescent cells, as evidenced by the transverse section shown in Fig. 5(c), displaying cells of various sizes. The inner nuclear layer (INL) emits the weakest signal, and is then not imaged here. Finally, the inner plexiform layer (IPL), although emitting a low fluorescence signal, allowed to single out individual cones, as showed in the transverse section in Fig. 5(d).

Lastly, 3PEF imaging on unlabeled fresh human colon was performed at  $\lambda_{\text{exc}} = 1700$  nm in Fig. 5(e), where the histological organization is displayed, even if individual cells are not perceptible.

Excitation wavelengths of  $\lambda_{\text{exc}} = 1300$  nm and  $\lambda_{\text{exc}} = 1700$  nm were chosen as these are considered ideal for 3PEF [12]. 3PEF imaging at  $\lambda_{\text{exc}} = 1300$  nm was performed with a  $565 \pm 66$  nm bandpass filter in front of the photomultiplier to target the green fluorescent protein (GFP) emission spectrum, whereas at  $\lambda_{\text{exc}} = 1700$  nm, the emission spectrum corresponds to higher wavelengths and was collected with a  $630 \pm 46$  nm bandpass filter.

### 6.3. Multimodal endoscope

The endoscope was designed to enable all kinds of multiphoton imaging techniques, and we demonstrate it in Fig. 6. First, Fig. 6(a) shows a composite image of the epidermal layer of unstained mouse skin using SHG (green) at  $\lambda_{\text{exc}} = 920$  nm, 3PEF (red) and THG (blue) at  $\lambda_{\text{exc}} = 1300$  nm. All three images were acquired one after the other and then stacked together. The collagen fibrils structure, emitting a strong SHG signal, is clearly visible, while 3PEF and THG



images provide information on the surrounding cellular structure. We further emphasize on the multimodality of the endoscope with label-free images of fresh human colon using THG at  $\lambda_{\text{exc}} = 1300$  nm in Fig. 6(b).

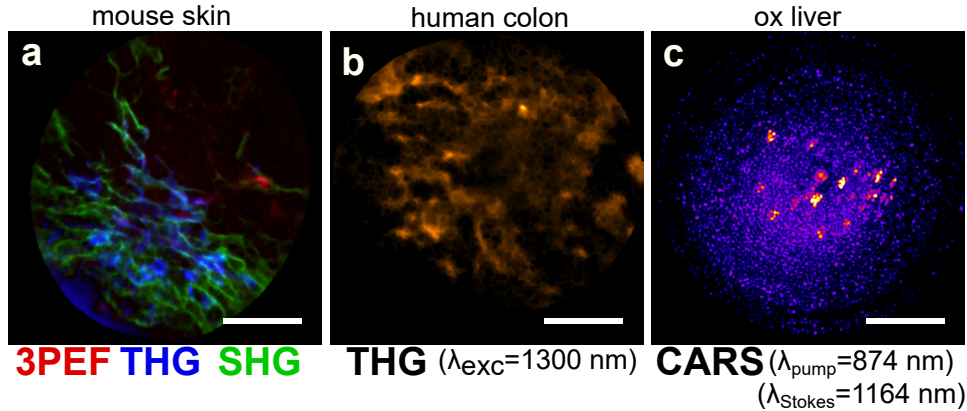


**Fig. 6.** (a) Composite 3PEF (red), THG (blue) and SHG (green) image of unstained mouse skin ( $\lambda_{\text{exc}} = 1300$  nm and mean power on the sample is 17 mW for 3PEF and THG, and  $\lambda_{\text{exc}} = 920$  nm and mean power on the sample is 11 mW for SHG), (b) THG ( $\lambda_{\text{exc}} = 1300$  nm and mean power on the sample is 32 mW), and (c) CARS ( $\lambda_{\text{pump}} = 874$  nm, and  $\lambda_{\text{Stokes}} = 1164$  nm, mean power on the sample is 12 mW) images of fresh unstained ox liver at a depth of 3 mm (endoscope inserted into the tissue). All images have been acquired with a 2 fps acquisition rate and averaged over 10 images, scale bar is 50  $\mu\text{m}$ .

To ensure the separation of the nonlinear signals collected, and along with the excitation wavelength adjustment, different filters were placed in the detection channel : a  $565 \pm 66$  nm bandpass filter for 2PEF at  $\lambda_{\text{exc}} = 920$  nm and 3PEF at  $\lambda_{\text{exc}} = 1300$  nm, a  $447 \pm 60$  nm bandpass filter for SHG and THG at the same wavelengths, a  $630 \pm 46$  nm bandpass filter for 3PEF and a  $562 \pm 20$  nm bandpass filter for THG at  $\lambda_{\text{exc}} = 1700$  nm.

#### 6.4. CARS endoscopic imaging

In addition to previously mentioned imaging techniques, we also performed CARS imaging using the same endoscope. For that, a Ti:Sa laser (Chameleon, Coherent) pumping an optical parametric oscillator (Chameleon compact OPO, A.P.E) was used, providing 125 fs pulses (FWHM) at a repetition rate of 80 MHz at  $\lambda_{\text{pump}} = 874$  nm and 250 fs pulses (FWHM) at  $\lambda_{\text{Stokes}} = 1164$  nm. The wavelengths were chosen to excite  $\text{CH}_2$  and  $\text{CH}_3$  chemical bonds around  $2850 \text{ cm}^{-1}$  and a CARS signal generated at a 700 nm wavelength (a  $700 \pm 20$  nm bandpass filter is placed before the detector). A delay line was placed on the Stokes beam path to synchronize pump and Stokes pulses. The synchronization was done with a cross-correlation measurement using two-photon absorption in a silicon photodiode at the endoscope output.

In a first set of experiments, we optimized the delay between pump and Stokes pulses in order to generate and collect a CARS signal inside olive oil (placed at the endoscope output) of about 3.5 M counts/s for a total average power of 75 mW on the sample. With the same average power, the signal collected without a sample, which is believed to be mainly caused by parasitic four wave mixing [49] in the GRIN micro-objective, was 80 k counts/s, granting a SNR of 43.75. A slight change in delay resulted in a significant increase of noise due to synchronization of both pulses in the GRIN micro-objective, rather than at the endoscope output.

We used this endoscope to take CARS images of fresh and unstained ox liver. To demonstrate deep tissue imaging, the endoscopic head was inserted manually about 3 mm deep into the liver

sample. Figure 6(c) shows an example of a CARS image acquired at 2 fps in these conditions, with a pump and Stokes power of respectively 5 and 7 mW on the sample. Lipid droplets that are abundant in liver tissue are clearly visible, highlighting the efficiency of our system to perform CARS imaging and its ability to make images by manipulating the endoscope manually into the tissue.

## 7. Discussion and summary

2PEF and 3PEF modalities provide the same chemical information on biological samples, but 3PEF allows a much higher transverse and axial resolution over 2PEF, as well as improved SNR, as demonstrated in Section 5 and Fig. 4. In addition, because of the higher excitation wavelengths and the fact that they are in the range that presents the better compromise between water absorption and tissue scattering [12], 3PEF also enables in principle to image much deeper in the tissues than 2PEF [19]. This particular feature could not be demonstrated here since the working distance of the GRIN micro-objective, which is 225  $\mu\text{m}$  in air or 300  $\mu\text{m}$  in water, is not large enough to allow light to penetrate deeper in the tissue. This will be a possible way of improvement in the near future.

Moreover, the PSF of our system, which was measured at 1.1  $\mu\text{m}$  FWHM at 920 nm, is not diffraction-limited, given the theoretical 0.7 object NA of the GRIN micro-objective (on the biological sample side). To understand this, let us focus on the spot after the GRIN fiber spliced to the hollow core fiber. This spot FWHM is 3.7  $\mu\text{m}$ , which corresponds to a  $1/e^2$  radius of 3.14  $\mu\text{m}$ . From Gaussian optics laws, the divergence of the beam after the focal spot is 0.093 rad, which is significantly less than the 0.15 NA of this side of the GRIN micro-objective. As a consequence, the input pupil of the GRIN micro-objective is not filled, which means that its output 0.7 NA is not filled and thus the output PSF is not diffraction-limited. To improve this, it would be possible to adjust the GRIN fiber parameters (length and core diameter) so that the divergence of the output beam reaches 0.15, to match the input NA of the GRIN micro-objective, but this would reduce the spot size, and enhance the parasitic THG signal discussed in section 3. The length of the GRIN fiber was optimized to find the best compromise between small spot size and reduced parasitic THG signal. Further developments will be required to optimize this and improve the final PSF of the endoscope.

In summary, we developed a highly multimodal nonlinear micro-endoscope capable of 3PEF imaging in addition to 2PEF, SHG, THG and CARS imaging modalities. It uses a double clad antiresonant hollow core fiber enabling transmission of ultrashort pulses over the 850-1700 nm spectral band with negligible spectral and temporal distortion. The output mode is shaped with a GRIN fiber specifically designed to reduce the nonlinear noise. Coupled with a GRIN micro-objective, it allows to reach a 1.1  $\mu\text{m}$  spot size for high resolution nonlinear imaging. The fiber also features a large silica double clad with a NA (0.38) to efficiently collect the nonlinear signals. Multiphoton images with a FoV of up to 200  $\mu\text{m}$  are obtained by scanning the output focused spot on the sample with a resonant piezoelectric tube. All combined, these features provide a flexible nonlinear micro-endoscope with a 3 mm large and 35 mm long distal head. Finally we demonstrate the multimodality of the endoscope with label-free images of several biological tissues, fresh and fixed, using different contrast mechanisms (2PEF, 3PEF, SHG, THG, CARS). This is to our knowledge the first micro-endoscope capable of nonlinear imaging with these five different modalities.

Our developed highly multimodal nonlinear endoscope platform has wide applications for various communities, ranging from biology research such as high-resolution real-time investigation of neuronal activity in the brain, to medical applications. It also opens the way to intraoperative label free investigation with tremendous impact on clinical cancer diagnosis.

**Funding.** Institut National de la Santé et de la Recherche Médicale (18CP128-00, PC201508); Aix-Marseille Université (A-M-AAP-ID-17-13-170228-15.22-RIGNEAULT); Région Hauts-de-France; Ministère de l'Éducation Nationale, de

l'Enseignement Supérieur et de la Recherche; National Institutes of Health (NIH R21 EY029406-01); Agence Nationale de la Recherche (ANR-11-IDEX-0001-02, ANR-19-CE19-0019-03, ANR-21-ESRE-0003, ANR-21-ESRS-0002).

**Acknowledgments.** The fiber was made at FiberTech Lille. We acknowledge Esben Andresen and Frédéric Louradour for fruitful discussions. We acknowledge R. Torero, A. Barras, and M. Bastide for giving access to the biological samples. The reported studies have been conducted following the EU ethical rules on animal. Colon tissue samples are coming from the Biobank of the Assistance Publique des hôpitaux de Marseille (AP-HM) – Marseille – FRANCE. The AP-HM biobank is open to research projects and administrated by an executive and ethic committee. Mouse brain slices are coming from the Institut des Neurosciences de la Méditerranée following INMED agreement number B13-055-19 and OGM agreement number 5817.

**Disclosures.** The authors declare no conflicts of interest.

**Data availability.** Data underlying the results presented in this paper may be obtained from the authors upon reasonable request.

**Supplemental document.** See [Supplement 1](#) for supporting content.

## References

1. M. Wagner, C. Redaelli, M. Lietz, C. A. Seiler, H. Friess, and M. W. Büchler, "Curative resection is the single most important factor determining outcome in patients with pancreatic adenocarcinoma," *Br. J. Surg.* **91**(5), 586–594 (2004).
2. W. Denk, J. H. Strickler, and W. W. Webb, "Two-photon laser scanning fluorescence microscopy," *Science* **248**(4951), 73–76 (1990).
3. M. Jain, N. Narula, A. Aggarwal, B. Stiles, M. M. Shevchuk, J. Sterling, B. Salamon, V. Chandel, W. W. Webb, N. K. Altorki, and S. Mukherjee, "Multiphoton Microscopy: A Potential "Optical Biopsy" Tool for Real-Time Evaluation of Lung Tumors Without the Need for Exogenous Contrast Agents," *Arch. Pathol. & Lab. Medicine* **138**(8), 1037–1047 (2014).
4. T. Pham, B. Banerjee, B. Crome, S. Mehravar, B. Skovan, H. Chen, and K. Kieu, "Feasibility of multimodal multiphoton microscopy to facilitate surgical margin assessment in pancreatic cancer," *Appl. Opt.* **59**(22), G1–G7 (2020).
5. K. Harpel, R. D. Baker, B. Amirsolaimani, S. Mehravar, J. Vagner, T. O. Matsunaga, B. Banerjee, and K. Kieu, "Imaging of targeted lipid microbubbles to detect cancer cells using third harmonic generation microscopy," *Biomed. Opt. Express* **7**(7), 2849 (2016).
6. N. V. Kuzmin, P. Wesseling, P. C. d. W. Hamer, D. P. Noske, G. D. Galgano, H. D. Mansvelder, J. C. Baayen, and M. L. Groot, "Third harmonic generation imaging for fast, label-free pathology of human brain tumors," *Biomed. Opt. Express* **7**(5), 1889 (2016).
7. S. Mehravar, B. Banerjee, H. Chatrath, B. Amirsolaimani, K. Patel, C. Patel, R. A. Norwood, N. Peyghambarian, and K. Kieu, "Label-free multi-photon imaging of dysplasia in Barrett's esophagus," *Biomed. Opt. Express* **7**(1), 148 (2016).
8. S. W. Hell, K. Bahlmann, M. Schrader, A. Soini, H. M. Malak, I. Gryczynski, and J. R. Lakowicz, "Three-photon excitation in fluorescence microscopy," *J. Biomed. Opt.* **1**(1), 71–74 (1996).
9. D. L. Wokosin, V. E. Centonze, S. Crittenden, and J. White, "Three-photon excitation fluorescence imaging of biological specimens using an all-solid-state laser," *Bioimaging* **4**(3), 208–214 (1996).
10. C. Xu, W. Zipfel, J. B. Shear, R. M. Williams, and W. W. Webb, "Multiphoton fluorescence excitation: New spectral windows for biological nonlinear microscopy," *Proc. Natl. Acad. Sci.* **93**(20), 10763–10768 (1996).
11. C. Xu and W. W. Webb, "Measurement of two-photon excitation cross sections of molecular fluorophores with data from 690 to 1050 nm," *J. Opt. Soc. Am. B* **13**(3), 481–491 (1996).
12. N. Horton, K. Wang, D. Kobat, C. Clark, F. Wise, C. Schaffer, and C. Xu, "In vivo three-photon microscopy of subcortical structures within an intact mouse brain," *Nat. Photonics* **7**(3), 205–209 (2013).
13. S. Witte, A. Negrean, J. C. Lodder, C. P. J. de Kock, G. Testa Silva, H. D. Mansvelder, and M. Louise Groot, "Label-free live brain imaging and targeted patching with third-harmonic generation microscopy," *Proc. Natl. Acad. Sci.* **108**(15), 5970–5975 (2011).
14. P. Theer, M. T. Hasan, and W. Denk, "Two-photon imaging to a depth of 1000  $\mu\text{m}$  in living brains by use of a  $\text{Ti}:\text{Al}_2\text{O}_3$  regenerative amplifier," *Opt. Lett.* **28**(12), 1022–1024 (2003).
15. D. G. Ouzounov, T. Wang, M. Wang, D. D. Feng, N. G. Horton, J. C. Cruz-Hernández, Y.-T. Cheng, J. Reimer, A. S. Tolias, N. Nishimura, and C. Xu, "In vivo three-photon imaging of activity of GCaMP6-labeled neurons deep in intact mouse brain," *Nat. Methods* **14**(4), 388–390 (2017).
16. T. Wang, D. G. Ouzounov, C. Wu, N. G. Horton, B. Zhang, C.-H. Wu, Y. Zhang, M. J. Schnitzer, and C. Xu, "Three-photon imaging of mouse brain structure and function through the intact skull," *Nat. Methods* **15**(10), 789–792 (2018).
17. M. Yildirim, H. Sugihara, P. T. C. So, and M. Sur, "Functional imaging of visual cortical layers and subplate in awake mice with optimized three-photon microscopy," *Nat. Commun.* **10**(1), 177 (2019).

18. A. Klioutchnikov, D. J. Wallace, M. H. Frosz, R. Zeltner, J. Sawinski, V. Pawlak, K.-M. Voit, P. S. J. Russell, and J. N. D. Kerr, "Three-photon head-mounted microscope for imaging deep cortical layers in freely moving rats," *Nat. Methods* **17**(5), 509–513 (2020).
19. T. Wang, T. Wang, and C. Xu, "Three-photon neuronal imaging in deep mouse brain," *Optica* **7**(8), 947–960 (2020).
20. S. Tang, W. Jung, D. T. McCormick, T. Xie, J. Su, Y.-C. Ahn, B. J. Tromberg, and Z. Chen, "Design and implementation of fiber-based multiphoton endoscopy with microelectromechanical systems scanning," *J. Biomed. Opt.* **14**(3), 034005 (2009).
21. M. T. Myaing, D. J. MacDonald, and X. Li, "Fiber-optic scanning two-photon fluorescence endoscope," *Opt. Lett.* **31**(8), 1076 (2006).
22. D. Do, H. Yoo, and D.-G. Gweon, "Fiber-optic raster scanning two-photon endomicroscope using a tubular piezoelectric actuator," *J. Biomed. Opt.* **19**(6), 066010 (2014).
23. V. Kučikas, M. P. Werner, T. Schmitz-Rode, F. Louradour, and M. A. M. J. van Zandvoort, "Two-Photon Endoscopy: State of the Art and Perspectives," *Mol. Imaging Biol.* (2021).
24. W. Liang, G. Hall, B. Messerschmidt, M.-J. Li, and X. Li, "Nonlinear optical endomicroscopy for label-free functional histology in vivo," *Light: Sci. Appl.* **6**(11), e17082 (2017).
25. H.-C. Park, H. Guan, A. Li, Y. Yue, M.-J. Li, H. Lu, and X. Li, "High-speed fiber-optic scanning nonlinear endomicroscopy for imaging neuron dynamics in vivo," *Opt. Lett.* **45**(13), 3605 (2020).
26. G. Ducourthial, P. Leclerc, T. Mansuryan, M. Fabert, J. Brevier, R. Habert, F. Braud, R. Batrin, C. Vever-Bizet, G. Bourg-Heckly, L. Thiberville, A. Druilhe, A. Kudlinski, and F. Louradour, "Development of a real-time flexible multiphoton microendoscope for label-free imaging in a live animal," *Sci. Rep.* **5**(1), 18303 (2015).
27. H. Guan, D. Li, H.-c. Park, A. Li, Y. Yue, Y. A. Gau, M.-J. Li, D. E. Bergles, H. Lu, and X. Li, "Deep-learning two-photon fiberscopy for video-rate brain imaging in freely-behaving mice," *Nat. Commun.* **13**(1), 1534 (2022).
28. Y. Wu, Y. Leng, J. Xi, and X. Li, "Scanning all-fiber-optic endomicroscopy system for 3D nonlinear optical imaging of biological tissues," *Opt. Express* **17**(10), 7907 (2009).
29. K. Murari, Y. Zhang, S. Li, Y. Chen, M.-J. Li, and X. Li, "Compensation-free, all-fiber-optic, two-photon endomicroscopy at 155 Mm," *Opt. Lett.* **36**(7), 1299 (2011).
30. A. Lombardini, V. Mytskaniuk, S. Sivankutty, E. R. Andresen, X. Chen, J. Wenger, M. Fabert, N. Joly, F. Louradour, A. Kudlinski, and H. Rigneault, "High-resolution multimodal flexible coherent Raman endoscope," *Light: Sci. Appl.* **7**(1), 10 (2018).
31. A. Kudlinski, A. Cassez, O. Vanvincq, D. Septier, A. Pastre, R. Habert, K. Baudelle, M. Douay, V. Mytskaniuk, V. Tsvirkun, H. Rigneault, and G. Bouwmans, "Double clad tubular anti-resonant hollow core fiber for nonlinear microendoscopy," *Opt. Express* **28**(10), 15062–15070 (2020).
32. A. Lukic, S. Dochow, H. Bae, G. Matz, I. Latka, B. Messerschmidt, M. Schmitt, and J. Popp, "Endoscopic fiber probe for nonlinear spectroscopic imaging," *Optica* **4**(5), 496–501 (2017).
33. E. Pshenay-Severin, H. Bae, K. Reichwald, G. Matz, J. Bierlich, J. Kobelke, A. Lorenz, A. Schwuchow, T. Meyer-Zedler, M. Schmitt, B. Messerschmidt, and J. Popp, "Multimodal nonlinear endomicroscopic imaging probe using a double-core double-clad fiber and focus-combining micro-optical concept," *Light: Sci. Appl.* **10**(1), 207 (2021).
34. D. Huland, K. Charan, D. Ouzounov, J. Jones, N. Nishimura, and C. Xu, "Three-photon excited fluorescence imaging of unstained tissue using a GRIN lens endoscope," *Biomed. Opt. Express* **4**(5), 652–658 (2013).
35. F. Akhouni, Y. Qin, N. Peyghambarian, J. K. Barton, and K. Kieu, "Compact fiber-based multi-photon endoscope working at 1700 nm," *Biomed. Opt. Express* **9**(5), 2326–2335 (2018).
36. M. Wang, M. Kim, F. Xia, and C. Xu, "Impact of the emission wavelengths on in vivo multiphoton imaging of mouse brains," *Biomed. Opt. Express* **10**(4), 1905–1918 (2019).
37. C. Wang, H. Liu, H. Liu, J. Ma, H. Cui, Y. Li, D. Wu, Y. Hu, D. Wu, D. Wu, Q. Fu, L. Liang, F. Yu, R. Wu, A. Wang, L. Feng, and L. Feng, "Spiral scanning fiber-optic two-photon endomicroscopy with a double-cladding antiresonant fiber," *Opt. Express* **29**(26), 43124–43135 (2021).
38. P. Uebel, M. C. Günendi, M. H. Frosz, G. Ahmed, N. N. Edavalath, J.-M. Ménard, and P. S. J. Russell, "Broadband robustly single-mode hollow-core PCF by resonant filtering of higher-order modes," *Opt. Lett.* **41**(9), 1961–1964 (2016).
39. C. Wei, R. J. Weiblen, C. R. Menyuk, and J. Hu, "Negative curvature fibers," *Adv. Opt. Photonics* **9**(3), 504–561 (2017).
40. B. Debord, A. Amsanpally, M. Chafer, A. Baz, M. Maurel, J. M. Blondy, E. Hugonnot, F. Scol, L. Vincetti, F. Gérôme, and F. Benabid, "Ultralow transmission loss in inhibited-coupling guiding hollow fibers," *Optica* **4**(2), 209–217 (2017).
41. M. Tateda, N. Shibata, and S. Seikai, "Interferometric method for chromatic dispersion measurement in a single-mode optical fiber," *IEEE J. Quantum Electron.* **17**(3), 404–407 (1981).
42. M. Zeisberger and M. A. Schmidt, "Analytic model for the complex effective index of the leaky modes of tube-type anti-resonant hollow core fibers," *Sci. Rep.* **7**(1), 11761 (2017).
43. P. Ferrand, J. Wenger, A. Devilez, M. Pianta, B. Stout, N. Bonod, E. Popov, and H. Rigneault, "Direct imaging of photonic nanojets," *Opt. Express* **16**(10), 6930–6940 (2008).
44. P. Ghenuche, H. Rigneault, and J. Wenger, "Photonic nanojet focusing for hollow-core photonic crystal fiber probes," *Appl. Opt.* **51**(36), 8637–8640 (2012).
45. K. Iga, "Theory for gradient-index imaging," *Appl. Opt.* **19**(7), 1039–1043 (1980).

46. M. Guizar-Sicairos and J. C. Gutiérrez-Vega, "Computation of quasi-discrete Hankel transforms of integer order for propagating optical wave fields," *J. Opt. Soc. Am. A* **21**(1), 53–58 (2004).
47. I. Raymond, A. Vila, U.-C. Huynh, and N. Brecha, "Cyan fluorescent protein expression in ganglion and amacrine cells in a thy1-CFP transgenic mouse retina," *Mol. Vision* **14**, 1559 (2008).
48. T. Vardi, M. Fina, L. Zhang, A. Dhingra, and N. Vardi, "mGluR6 Transcripts in Non-neuronal Tissues," *J. Histochem. Cytochem.* **59**(12), 1076–1086 (2011).
49. A. Lombardini, E. R. Andresen, A. Kudlinski, I. Rimke, and H. Rigneault, "Origin and suppression of parasitic signals in Kagomé lattice hollow core fibers used for SRS microscopy and endoscopy," *Opt. Lett.* **42**(9), 1824–1827 (2017).